Volume 1 | Number 1 | Jan 2013 | Pages 1–100

Dalton Transactions

An international journal of inorganic chemistry
www.rsc.org/dalton

ROYAL SOCIETY OF CHEMISTRY

ROYAL SOCIETY OF CHEMISTRY

www.rsc.org/dalton

Heterometallic Trinuclear {Co$^{III}_2$Ln^{III}} (Ln = Gd, Tb Ho and Er) Complexes in a Bent Geometry. Field-induced Single-Ion Magnet Behavior of the Er^{III} and Tb^{III} Analogues

*Joydeb Goura,[a] Jamie Brambleby,[b] Craig V. Topping,[c] Paul A. Goddard,[*b] Ramakirushnan Suriya Narayanan,[d] Arun Kumar Bar[d] and Vadapalli Chandrasekhar*[a,d]*

[a]Department of Chemistry, Indian Institute of Technology Kanpur, Kanpur-208016, India;

[b]Department of Physics, University of Warwick, Gibbet Hill Road, Coventry, CV4 7AL, United Kingdom;

[c]Department of Physics, Clarendon Laboratory, University of Oxford, Oxford, Parks Road, OX1 3PU, United Kingdom;

[d]National Institute of Science Education and Research, Institute of Physics Campus, Sachivalaya Marg, Sainik School, Bhubaneswar, Orissa - 751 005, India

E-mail: vc@iitk.ac.in; vc@niser.ac.in;

p.goddard@warwick.ac.uk

Abstract

Through the use of a multi-site compartmental ligand, 2-methoxy-6-[{2-(2-hydroxyethylamino)ethylimino}methyl] phenol (LH$_3$), the family of heterometallic, trinuclear complexes of formula [Co$^{III}_2$Ln(L)$_2$(μ-O$_2$CCH$_3$)$_2$(H$_2$O)$_3$]$^.$NO$_3^.$xMeOH$^.$yH$_2$O has been expanded beyond Ln = Dy^{III} to include Gd^{III} (**1**), Tb^{III} (**2**), Ho^{III} (**3**) and Er^{III} (**4**) for **1,3** and **4** (x= 1; y = 1) and for **2** (x = 0; y = 2). The metallic core of these complexes consist of a (Co^{III}-Ln^{III}-Co^{III}) motif bridged in a bent geometry resulting in six-coordinated distorted Co^{III} octahedra and nine-coordinated Ln^{III} monocapped square-antiprisms. Magnetic characterization of these compounds reveals the erbium and terbium analogues to display field induced single-ion magnetic behavior similar to the dysprosium analogue but at lower temperatures. The energy barrier for the reversal of the magnetization of Co$^{III}_2$Tb^{III} analogue is $U_{eff} \geq 15.6(4)$ K, while for the Co$^{III}_2$Er^{III} analogue $U_{eff} \geq 9.9(8)$ K. The magnetic properties are discussed in terms of distortions of the 4f electron cloud.

Introduction

Heterometallic polynuclear complexes particularly those containing 3d/4f metal ions have

been receiving increasing attention in recent years, especially because of their interesting

magnetic properties arising out of the interaction between the paramagnetic 3d and the 4f

metal ions suggesting possible applications in information storage, magnetic refrigeration and

quantum computing.[1] Members of this family have been shown to be single-molecule

magnets (SMMs) and are particularly intriguing as an avenue towards high density

information storage and spintronics[1] Furthermore, they are also known to display the property

of quantum tunnelling of magnetization (QTM).[1] A recent development in this area has been

realization that replacement of the paramagnetic 3d metal ion by a diamagnetic species can

lead, in some instances, to complexes with better magnetic properties.[2] In such cases, where

SMM behaviour is seen, the complexes are called single-ion-magnets (SIMs) since the

magnetic properties are essentially deemed to be derived from the lanthanide metal ion.[2]

Theoretical studies, by Rajaraman[3] and co-workers have revealed that the role of the

diamagnetic metal ion is to make the oxide ligands more hard and hence allow a tighter

binding with the lanthanide metal ion causing a substantial energy separation between the

ground and excited electronic states of the latter. Previously, we have utilized the

phosphorus-supported ligand $SP[N(Me)N=CH-C_6H_3-2-OH-3-OMe]_3$ for the preparation of

heterometallic trinuclear complexes (Chart 1) which showed SMMs properties.[4] Interestingly,

in these complexes, the arrangement of the trimetallic core is perfectly linear. Also the 3d

metal ions are paramagnetic. More recently, in a preliminary communication, we reported a

heterometallic, $\{Co^{III}_2Dy\}$ complex, containing diamagnetic Co^{III} ions that showed SMM

behaviour.[5] We now report the full details of these studies. Accordingly, the synthesis,

structure and magnetism of $[Co^{III}_2Ln(L)_2(\mu-O_2CCH_3)_2(H_2O)_3]\cdot NO_3\cdot xMeOH\cdot yH_2O$ [Ln = Gd^{III}

(**1**), Tb^{III} (**2**), Ho^{III} (**3**) and Er^{III} (**4**) for **1,3** and **4** (x= 1; y = 1) and for **2** (x = 0; y = 2)] are

reported herein. All the complexes (**1-4**) possess a bent trimetallic {Co$^{III}_2$Ln} motif. Among these complexes, the Er^{III} and Tb^{III} analogue shows a field-induced SIM behavior. In general, SMMs containing Er^{III} are quite rare. Recently Dunbar et al have reported a mononuclear four-coordinate Er^{III} complex that was shown to be a SMM.[6]

Experimental Section

Reagents and General Procedures

Solvents and other general reagents used in this work were purified according to standard procedures.[7] Co(OAc)$_2$·4H$_2$O, *N*-(2-hydroxyethyl)ethylenediamine and *o*-vanillin were obtained from S.D. Fine Chemicals, India. Gd(NO$_3$)$_3$·6H$_2$O, Tb(NO$_3$)$_3$·5H$_2$O, Ho(NO$_3$)$_3$·5H$_2$O and Er(NO$_3$)$_3$·5H$_2$O were obtained from Sigma Aldrich (U.S.A.) and used as received. The ligand 2-methoxy-6-[{2-(2-hydroxyethylamino)ethylimino}methyl] phenol (LH$_3$) was prepared by a reported procedure.[5,8]

Instrumentation

Melting points were measured using a JSGW melting point apparatus and are uncorrected. IR spectra were recorded as KBr pellets on a Bruker Vector 22 FT IR spectrophotometer operating at 400-4000 cm^{-1}. Elemental analyses of the compounds were obtained from Thermoquest CE instruments CHNS-O, EA/110 model. Electrospray ionization mass spectrometry (ESI-MS) spectra were recorded on a Micromass Quattro II triple quadrupole mass spectrometer. ^{1}H NMR spectra were recorded in CDCl$_3$ solutions on a JEOL JNM LAMBDA 400 model spectrometer operating at 400.0 MHz. Chemical shifts are reported in parts per million (ppm) and referenced with respect to internal tetramethylsilane (^{1}H).

DC Magnetometry:

Powdered samples of Co$_2$Gd, Co$_2$Tb, Co$_2$Ho and Co$_2$Er were dispersed in Vaseline to prevent the samples from moving and placed inside a gelatin capsule. The capsule was fixed inside a plastic drinking straw and attached to the end of a brass rod. The sample's magnetic moment

(M) was then measured in an applied field of $\mu_0 H = 0.1$ T for temperatures in the range 1.8 $\leq T \leq$ 300 K, with a Quantum Design SQUID magnetometer. In the linear limit, the molar susceptibility (χ_{mol}) was deduced from this measurement using $\chi_{mol} = M/nH$, where n is the number of moles of the sample. An isothermal measurement of the magnetic moment at 2 K was also recorded for applied fields up to $\mu_0 H = 7$ T.

AC susceptibility:

AC susceptibility measurements were performed on powdered samples. For Co_2Gd measurements were recorded on cooling from 10 K with the AC Measurement System insert to a Quantum Design Physical Property Measurement System at the University of Oxford. An AC field of amplitude $\mu_0 H_{AC} = 0.4$ mT and frequencies in the range 15 $\leq f \leq$ 1500 Hz was applied, and data were recorded in DC fields of $\mu_0 H_{DC} = 0$ and 0.1 T. In the case of Co_2Er, the frequency range was extended to 10 kHz to investigate the onset of SIM behaviour at low temperatures. This behaviour was also repeatable with a reduced AC-field amplitude, indicating no sample heating occurred on the application of the ac-field for the measurements presented in this study.

For Co_2Tb, AC measurements were performed in a Quantum Design PPMS at the Materials Characterisation Laboratory at the ISIS Neutron and Muon Source. Data were recorded in the frequency range 15 $\leq f \leq$ 10000 Hz for $\mu_0 H_{AC} = 0.4$ mT. Through a field-dependent study of the AC susceptibility at 2 K, we found it necessary to increase the DC-field above 0.1 T to induce maxima in the out-of-phase susceptibility component within the experimentally accessible temperature range. The temperature dependence of this sample was therefore performed in an applied fields of $\mu_0 H_{DC} = 0$ T and 0.15 T. The low temperature SIM behaviour observed in the latter case was reproducible when recorded with a reduced AC-field amplitude of 0.1 mT.

For the measurements performed in the PPMS, wait times extending up to 45 s were included following a change of the AC frequency during the measurement, to ensure reliability of the data across the measured frequency range.

For Co_2Ho, measurements were made with a Quantum Design SQUID magnetometer at the University of Oxford. The sample exhibited no field-induced slow relaxation for frequencies in the range $10 \leq f \leq 1000$ Hz and amplitude $\mu_0H_{AC} = 0.4$ mT, and with DC fields of $\mu_0H_{DC} = 0$ and 0.1 T.

X-ray Crystallography

Single-crystal X-ray structural studies of **1-4** were performed on a Bruker *SMART APEX* CCD diffractometer equipped with an Oxford low-temperature attachment. Data were collected using a graphite-monochromated MoK_α radiation ($\lambda_\alpha = 0.71073$ Å). The crystals did not degrade/decompose during the data collection. Data collection, reduction were performed using the *SMART*, *SAINT* programs respectively.[9a-c] The structure solving and refinement were performed using SHELXT and SHELXL-2014/7 programs[9d,e] on WinGX software package.[9f-h] Refinements were carried out with full-matrix least-squares methods against F^2. All of the hydrogen atoms were fixed at idealized positions and a riding model was used. The best fit models for the current data sets are satisfactorily good. Inspite of our best efforts to obtain the best quality data, the CH_2CH_2 moieties of the ligand and the interstitial solvent molecules are highly disordered. Hence, we had to employ restrains/constrains for disordered modeling. One of the C atoms in each of the CH_2CH_2 moieties is highly disorder in terms of thermal ellipsoid and hence it electron density was partitioned into two positions. In **2**, one such C atom with partial occupancy is modelled with isotropic displacement refinement. For each complex, the asymmetric unit contains one half-occupied NO_3 counter anion which is intertwined with one disordered water molecule. The intertwined disordered water molecule possesses four sites. The remaining solvent molecules

are too disordered to locate their positions and hence squeezed out using PLATON/SQUEEZE program.[9i]. The solvent accessible void volumes and possible squeezed out electron counts are described in corresponding CIFs. The crystallographic data in CIF formats are provided in ESI. Crystal data and refinement parameters are summarized Table 1. The selected bond parameters are sorted in Table S1 (ESI). The ORTEP diagrams of all the complexes are portrayed in Fig. 1 and the representative asymmetric unit is as shown in Fig. 2. All of the mean plane analyses and molecular drawings were obtained using Diamond (*version 3.2k*).[9j]

Table 1. Crystal data and structure refinement parameters of **1-4**

Compound	1	2	3	4
Formula[a]	$C_{31}H_{62}Co_2Gd$ N_5O_{23}	$C_{28}H_{58}Co_2Tb$ N_5O_{24}	$C_{32}H_{62}Co_2Ho$ N_5O_{22}	$C_{31}H_{64}Co_2Er$ N_5O_{24}
Formula weight[a]	1147.94	1125.14	1151.65	1175.98
Temp. (K)	298(2)	298(2)	298(2)	298(2)
Crystal system	Monoclinic	Monoclinic	Monoclinic	Monoclinic
Space group	*C2/c*	*C2/c*	*C2/c*	*C2/c*
a (Å)	25.139(5)	25.196(5)	25.251(5)	25.231(5)
b (Å)	11.924(5)	11.877(5)	11.921(5)	11.986(5)
c (Å)	16.545(5)	16.580(5)	16.799(5)	16.814(5)
α (°)	90	90	90	90
β (°)	116.956(5)	117.333(5)	117.387(5)	116.896(5)
γ (°)	90	90	90	90
Volume (Å^3); Z	4421(2); 4	4408(2); 4	4490(2); 4	4535(2); 4
Density(Mgm^{-3})	1.722	1.695	1.703	1.723
Abs. coef. (mm^{-1})	2.294	2.400	2.543	2.624
Reflections collected	19905	13959	19948	20011
Unique reflections [R_{int}]	5531 [0.0415]	5509 [0.0612]	5651 [0.0387]	5714 [0.0594]
Completenes (%) to θ (°)	99.8 to 28.366	92.9 to 28.344	99.5 to 28.399	99.9 to 28.443
GOOF on F^2	1.097	1.140	1.042	1.007
Final R indices: R_1[b] (wR_2[c])	0.0365 (0.1036)	0.0601 (0.1873)	0.0350 (0.097)	0.0432 (0.1194)
[a] the formula and the formula weights include the un-modelled H atoms and the masked solvent molecules also. [b] $R_1 = \sum|F_0 - F_c|/\sum F_0$; [c] $wR_2 = \sum[w(F_0^2 - F_0^2)]^2/[w(F_0^2)^2]^{\frac{1}{2}}$				

Synthesis

General Procedure for the synthesis of metal complexes 1-4

A general protocol was employed for the synthesis of the metal complexes (**1-4**) as follows. LH_3 (1 eq.) was dissolved in methanol (20 mL). $Ln(NO_3)_3 \cdot nH_2O$ (1 eq.) was added to this solution. The reaction mixture was stirred for 30 minutes. At this stage, $Co(OAc)_2 \cdot 4H_2O$ (2 eq.) and tetramethyl ammonium hydroxide (Me_4NOH) (2 eq.) were added to the reaction mixture and stirred for a further 12 hours at room temperature to afford a clear brown solution. Solvent was removed from the reaction mixture and the residue obtained was washed with diethyl ether, dried, re-dissolved in methanol, filtered and kept in a vial for crystallization. After 15 days, brown block-shaped crystals suitable for X-ray diffraction were isolated. Specific details of each reaction and the characterization data of the products obtained are given below.

$[Co^{III}_2Gd^{III}(L)_2(\mu-O_2CCH_3)_2(H_2O)_3]^.NO_3^.MeOH^.H_2O$ (1)

Quantities: $Co(OAc)_2 \cdot 4H_2O$ (0.130 g, 0.521 mmol), $Gd(NO_3)_3 \cdot 6H_2O$ (0.117 g, 0.260 mmol), LH_3 (0.062 g, 0.260 mmol) and Me_4NOH (0.047 g, 0.520 mmol). Yield: 0.122 g, 42 % (based on Gd). Mp: >230^{0}C. IR (KBr) cm^{-1}: 3394(br), 3296(br), 2395(w), 1762(w), 1645(m), 1559(s), 1472(m), 1383(s), 1297(s), 1245(m), 1224(s),1171(w), 1076(w), 1030(m), 966(m), 908(w), 864(w), 825(m), 785(w), 740(m), 683(m), 618(w), 519(w). ESI-MS m/z, ion: 1014.0833, $[Co^{III}_2Gd(L)_2(\mu-O_2CCH_3)_2(H_2O)_3 + 3CH_3OH]^+$. Anal. Calcd for $C_{29}H_{48}Co_2GdN_5O_{18}$(1029.84): C, 33.82; H, 4.70; N, 6.80. Found: C, 33.69; H, 4.54; N, 6.69.

$[Co^{III}_2Tb^{III}(L)_2(\mu-O_2CCH_3)_2(H_2O)_3]^.NO_3^.2H_2O$ (2)

Quantities: $Co(OAc)_2 \cdot 4H_2O$ (0.130 g, 0.521 mmol), $Tb(NO_3)_3 \cdot 5H_2O$ (0.113 g, 0.260 mmol), LH_2 (0.08 g, 0.29 mmol) and Me_4NOH (0.047 g, 0.520 mmol). Yield: 0.126 g, 43% (based on Tb). Mp: >230^{0}C. IR (KBr) cm^{-1}: 3408(s), 3276(br), 2854(w), 2396(w), 1763(w), 1646(s),1608(s), 1566(s), 1473(s), 1441(s), 1456(s),1383(s), 1295(s), 1246(m), 1224(s),

1171(w), 1076(w), 1051(m), 1030(m), 966(m), 941(w), 908(w), 865(w), 825(w), 786(w), 740(m), 685(w), 667(w), 636(w), 623(w), 598(w), 567(w), 541(w), 520(w), 474(w). ESI-MS m/z, ion: 960.0533, $[Co^{III}_2Tb(L)_2(\mu\text{-}O_2CCH_3)_2(H_2O)_3 + CH_3CN]^+$. Anal. Calcd for $C_{28}H_{46}Co_2TbN_5O_{18}$ (1017.48): C, 33.05; H, 4.56; N, 6.88. Found: C, 32.96; H, 4.41; N, 6.79.

$[Co^{III}_2Ho^{III}(L)_2(\mu\text{-}O_2CCH_3)_2(H_2O)_3]^{.}NO_3^{.}MeOH^{.}H_2O$ (3)

Quantities: $Co(OAc)_2 \cdot 4H_2O$ (0.130 g, 0.521 mmol), $Ho(NO_3)_3 \cdot 5H_2O$ (0.115 g, 0.26 mmol), LH_2 (0.062 g, 0.260 mmol) and Me_4NOH (0.047 g, 0.520 mmol). Yield: 0.128 g, 44 % (based on Ho). Mp: >230^0C. IR (KBr) cm^{-1}: 3394(br), 3200(br), 2395(w), 1762(w), 1644(w), 1559(s), 1383(s), 1246(m), 1224(m), 1171(w), 1077(w), 1028(m), 966(w), 908(w), 863(w), 825(m), 785(w), 740(w), 683(m), 617(w), 542(w). ESI-MS m/z, ion: 1112.0149, $[Co^{III}_2Ho(L)_2(\mu\text{-}O_2CCH_3)_2(H_2O)_3 + CH_3OH + 3H_2O]^+$. Anal. Calcd for $C_{29}H_{48}Co_2HoN_5O_{18}$ (1037.52): C, 33.57; H, 4.66; N, 6.75. Found: C, 33.45; H, 4.42; N, 6.69.

$[Co^{III}_2Er^{III}(L)_2(\mu\text{-}O_2CCH_3)_2(H_2O)_3]^{.}NO_3^{.}MeOH^{.}H_2O$ (4)

Quantities: $Co(OAc)_2 \cdot 4H_2O$ (0.130 g, 0.521 mmol), $Er(NO_3)_3 \cdot 5H_2O$ (0.115 g, 0.26 mmol), LH_2 (0.062 g, 0.260 mmol) and Me_4NOH (0.047 g, 0.520 mmol). Yield: 0.127 g, 43 % (based on Er). Mp: >230^0C. IR (KBr) cm^{-1}: 3395(br), 3260(br), 2856(w), 2395(w), 1762(w), 1647(m), 1607(m), 1566(s), 1473(m), 1383(s), 1296(s), 1246(s), 1224(s),1170(w), 1076(m), 1051(m), 966(m), 908(w), 865(w), 825(w), 785(w), 740(m), 687(w), 619(w), 598(w), 542(w), 523(w). ESI-MS m/z, ion: 926.0284, $[Co^{III}_2Er(L)_2(\mu\text{-}O_2CCH_3)_2(H_2O)_3]^+$. Anal. Calcd for $C_{29}H_{47}Co_2ErN_5O_{18}$ (1038.84): C, 33.53; H, 4.56; N, 6.74. Found: C, 33.41; H, 4.43; N, 6.64.

Results and discussion

Synthesis

Compartmental ligands containing *o*-vanillin have been shown to be effective for the preparation of the both heterometallic (3d/4f) or homometallic (3d and 4f) complexes.[10] The multi-site coordination ligand, derived from *o*-vanillin, 2-methoxy-6-[{2-(2-

hydroxyethylamino)ethylimino}methyl] phenol (LH_3) contains five coordination sites: one phenolic oxygen, one -OMe, one imino nitrogen and one secondary amine nitrogen along with a terminal, flexible, $-NCH_2CH_2OH$ arm. An examination of this ligand reveals the presence of two distinct coordination binding sites. While one of these sites is expected to prefer a transition metal ion, the other site, owing to the presence of the -OMe group is likely to bind to a lanthanide metal ion. This hypothesis was successfully tested by us earlier and involved the preparation of heterometallic $\{Fe^{III}_4Ln^{III}_2\}$[11] and $\{Co^{III}_2Dy^{III}\}$[5] complexes. Accordingly, the sequential reaction of 2-methoxy-6-[{2-(2-hydroxyethylamino)ethylimino} methyl] phenol (LH_3) with various lanthanides metal salts followed by the reaction with $Co(OAc)_2 \cdot 4H_2O$ in a 1:1:2 stoichiometric ratio in the presence of tetramethylammonium hydroxide (Me_4NOH) afforded trinuclear heterobimetallic Co_2Ln complexes with the general formula, $[Co^{III}_2Ln(L)_2(\mu\text{-}O_2CCH_3)_2(H_2O)_3]\cdot NO_3\cdot xMeOH\cdot yH_2O$ [Ln = Gd^{III} (**1**), Tb^{III} (**2**), Ho^{III} (**3**) and Er^{III} (**5**)] for **1,3** and **4** (x= 1; y = 1) and for **2** (x = 0; y = 2) (Scheme 1). The presence of Co^{III} in these complexes is attributed to the ready aerial oxidation of Co^{II}.

ESI-MS spectra of **1-4** reveal that they retain their molecular integrity in solution as indicated by the presence of parent ion peaks at m/z: 1014.0833, $[Co^{III}_2Gd(L)_2(\mu\text{-}O_2CCH_3)_2(H_2O)_3 + 3CH_3OH]^+$; 960.0533, $[Co^{III}_2Tb(L)_2(\mu\text{-}O_2CCH_3)_2(H_2O)_3 + CH_3CN]^+$; 1112.0149, $[Co^{III}_2Ho(L)_2(\mu\text{-}O_2CCH_3)_2(H_2O)_3 + CH_3OH + 3H_2O]^+$ and 926.0284, $[Co^{III}_2Er(L)_2(\mu\text{-}O_2CCH_3)_2(H_2O)_3]^+$ respectively. The ESI-MS spectrum of **1**, as a representative example, is given in Fig. 3a and 3b and those of the other complexes **2-4** are given in the Supporting Information.

Molecular structures of 1-4

The molecular structures of **1-4** were determined by single-crystal X-ray crystallography which reveals that these are isostructural. All the complexes crystallized in the monoclinic

system, *C2/c* (Z = 4). The crystallographic parameters of these complexes are given in Table 1. All the complexes are monocationic and contain nitrate counter anions. In view of the structural similarities of these complexes, the molecular structure of **1** is described as a representative example. The structural details of all other compounds are given in the Supporting Information.

The asymmetric unit of **1** contains half of the total molecule, namely, [CoGd(L)(μ-OAc)(OH$_2$)(OH$_{2/2}$)] (Chart 2 and Fig. 2). The molecular structure of **1** is given in Scheme 1 and Fig. 1. The various coordination modes of all the participating ligands in **1-4** are summarized in Chart 3. The trimetallic core of the complex contains a bent {Co^{III}$_2$Gd^{III}} motif with the Gd^{III} ion placed in the centre and connected on either side to a Co^{III} through the intervention of various bridging ligands viz., [NCH$_2$CH$_2$O]$^-$, a phenoxide and a acetate. The coordination around Co^{III} is completed by two ethylenediamino nitrogen atoms and a water molecule. The coordination around the central lanthanide is completed by the methoxide groups and one water molecule. It is interesting to compare the structural features of the current family of {Co^{III}$_2$Ln^{III}} complexes with the previously known {Co^{II}$_2$Ln^{III}}[4] complexes. In the latter the Co^{II} ion has a 3N, 3O coordination environment while the lanthanide ion has a 12 O environment. Also, in the latter, the central Ln^{III} is connected to the peripheral Co^{II} through three phenoxide bridges (Chart 1 and Table 2). The metric parameters involved in the current instance and in the literature examples are different and these values are summarized in Table 2. From these data we can see that the Co-N and Co-O bond distances are shorter in the current instance, because Co^{III} is involved, while in the reported case, because Co^{II} is present, these values are longer. On the other hand, Ln-O bond distances in the current instance and in the literature precedents are very similar. Most important variation, however, is in the geometry of the Co-Ln-Co motif. While in the present instance the geometry is bent and the Co-Ln-Co bond angles are in the range, 99.75(5)-100.81(4), in

$[L'Co^{II}LnCo^{II}L]$ ($L'H_3$ = SP[N(Me)N=CH-C_6H_3-2-OH-3-OMe]) the Co-Ln-Co geometry is perfectly linear. This difference is mainly because of the nature of the ligands involved. In the case of the phosphorus-supported ligand system the three hydrazone arms anchored to the phosphorus center force the linear geometry. The more flexible ligand, in the current instance, allows a more relaxed bent geometry.

Ln = Eu; Gd; Tb; Dy and Ho

X = Cl or NO$_3$
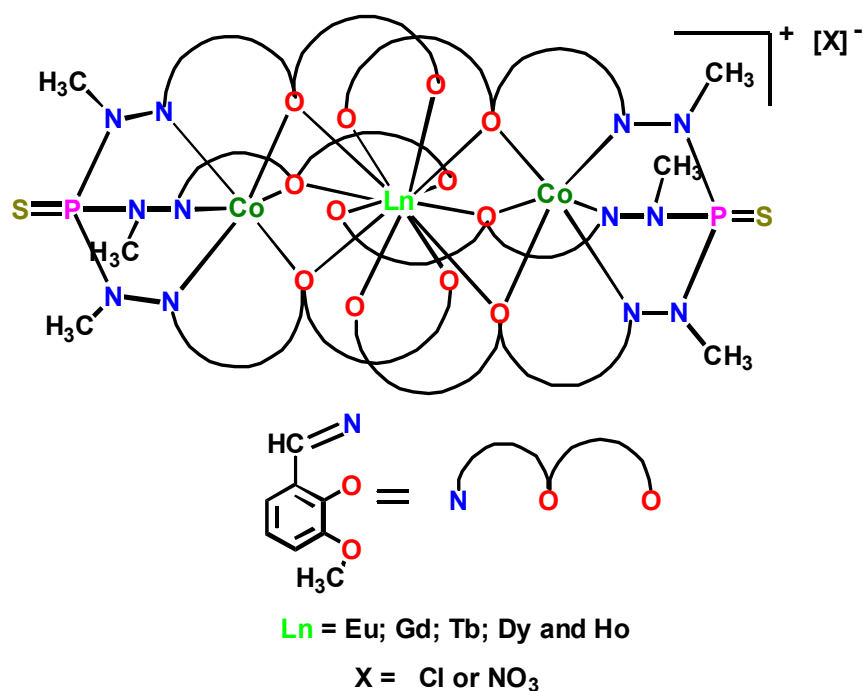
Chart 1. Previously known $Co^{II}_2Ln^{III}$ complexes.[4]

Table 2. Comparison of bond lengths (Å) and bond angles (°) between the trinuclear [Co^{III}-Ln^{III}-Co^{III}] complexes reported here and the earlier reported [Co^{II}-Ln^{III}-Co^{II}][4] complex.

Co/Ln-N/O$_{label}$ distance (Å)	[Co$^{III}_2$Ln(L)$_2$(O$_2$CCH$_3$)$_2$(H$_2$O)$_3$]·[NO$_3$] (This work)	[L$_2$Co$_2$Ln][NO$_3$] (ref. 4) (see Chart 1)
Co-N$_{imine}$	1.869(8)- 1.880(4)	2.096(6)-2.132(6)
Co-N$_{Secondary\ amine}$	1.903(3)- 1.920(7)	-
Co-O$_{phenolic}$	1.872(3)– 1.892(5)	2.076(4) - 2.107(4)
Co-O$_{terminal\ alkoxy}$	1.887(3)- 1.898(3)	-

Co-O$_{acetate}$	1.918(3)- 1.933(6)	-
Co-O$_{water}$	1.941(4)- 1.959(7)	-
Ln-O$_{terminal\ alkoxy}$	2.338(3)- 2.389(3)	-
Ln−O$_{phenolic}$	2.347(3)- 2.385(2)	2.363(5) - 2.396(3)
Ln-O$_{methoxy}$	2.687(3)- 2.706(3)	2.865(3) - 2.932(2)
Ln-O$_{acetate}$	2.312(3)- 2.360(3)	-
Ln-O$_{water}$	2.361(5)- 2.398(6)	-
Co-Ln	3.2923(9)- 3.3265(9)	3.269(9) – 3.310(9)
Co-Co	5.066(1)- 5.087(2)	6.538(1) – 6.621(1)
Angle (°)		
Co-Ln-Co	99.74(3)- 100.85(3)	180.00(2)
Co-O$_{phenolic}$-Ln	101.70(2)- 101.92(10)	94.31(2)-94.43(2)
Co-O$_{alkoxy}$-Ln	101.17(11)- 101.8(3)	-

A further description of the molecular structure of **1** is in order. Thus, it may be noticed that on either end a [L]$^{3-}$ ligand holds a dinuclear Gd-Co motif together. Thus, the methoxy group binds to the Gd^{III} centre (Gd1-O1, 2.687(3) Å) while the phenolate bridges a Co^{III} and the Gd^{III} ions [Co1-O2, 1.878(2) Å; Gd1-O2, 2.385(2) Å]. An imino nitrogen, is bound to a Co^{III} center [Co1-N1, 1.875(3) Å]. Interestingly, the secondary amine motif of the ligand is deprotonated in the presence of tetramethylammonium hydroxide and the resulting coordination center binds exclusively with Co^{III} [Co1-N2, 1.903(3) Å]. In addition, the asymmetric unit contains one η^1, η^1 coordinated acetate bridged ligands that bridge the Co/Gd pairs [Co1-O5, 1.923(3) Å; Gd1-O4, 2.360(3) Å]. Another interesting observation is that the terminal, flexible, -NCH$_2$CH$_2$OH arm (ethylenediamine motif) of the ligand is deprotonated under the reaction conditions and helps in bridging Co^{III} and Gd^{III} [Co1-O3, 1.898(3) Å; Gd1-O3, 2.389(3) Å]. The oxidation state of Co^{III} ions was confirmed by BVS analysis (Supporting Information).[12] Thus the two Co^{III} centers in **1** are equivalent and hexacoordinate (2N,4O) in a distorted octahedral geometry (Fig. 4a) and the Gd^{III} center is nine-coordinate in

a distorted monocapped square antiprism geometry (Fig. 4b). A mean plane analysis of core **1** reveals that two Co^{III} and Gd^{III} ions are present in the same plane (Fig. 5) and are arranged in the vertices of an isosceles triangle. The Co^{III}-Co^{III} bond distance is 5.086(2) Å while the Co^{III}-Gd^{III} distance is 3.325(1) Å.

Magnetic Studies

DC Magnetometry

The DC susceptibility of each sample, plotted as $\chi_{mol}T$ vs. T, is shown in Fig. 6a. The data have been corrected for core diamagnetism, estimated from the appropriate Pascal's constants.[13] In the high temperature limit, the samples have approximately constant values of $\chi_{mol}T$ indicating the moments are in the paramagnetic phase. The values of $\chi_{mol}T$ at 300 K are within approximately 10 % of that expected for independent lanthanide ions, $\mu_0 N_A \mu_{eff}^2 / 3k_B$, where $\mu_{eff} = g_J[J(J+1)]^{1/2}\mu_B$ is the effective moment (g_J is the Landé g-factor and J is the total-spin quantum number). This indicates that the magnetism in each sample is due to the lanthanide ions alone and that the octahedrally coordinated Co^{III} ions are in the low-spin ($S = 0$) state. The difference in the measured and expected moments is representative of the error in determining the mass of the powdered samples after dispersing them in Vaseline, and may also include a small diamagnetic contribution to the measurement from the sample holder and Vaseline.

For Co_2Gd, the flat response of $\chi_{mol}T$ down to low temperatures is indicative of paramagnetic moments. This is characteristic of Gd^{III} ions, in which the ground-state 4f $^8S_{7/2}$ multiplet has zero angular-momentum component and, as a result, a spherically symmetric electron distribution. The anisotropy of moments in lanthanide complexes arises from the lack of spherical asymmetry of the lanthanide ion's 4f electron wave functions in the presence of the ligand field,[14] which therefore implies the Gd^{III} moments will exhibit Heisenberg behaviour.

If exchange interactions were present between Gd^{III} ions, $\chi_{mol}T$ would deviate away from a horizontal line (see e.g. ref. 15). The flat form of $\chi_{mol}T$ therefore also suggests that exchange interactions between the Gd^{III} ions are weak. Given that Gd^{III} contains the maximum number of unpaired electrons in the 4f orbitals of any lanthanide ion, the implication is that spin-density may become delocalised in more directions in the crystal compared to the Tb^{III}, Ho^{III} and Er^{III} congeners. This suggests that each of these remaining members of this isotructual series are also likely to have weak exchange interactions between lanthanide ions, such that the magnetic properties of Co_2Tb, Co_2Ho and Co_2Er are dominated by single-ion behaviour.

In the case of Tb^{III}, Ho^{III} and Er^{III}, the product $\chi_{mol}T$ begins to decrease from its high temperature value below about 100 K. This is attributed to the thermal depopulation of crystalline-electric field (CEF) splitting of the lanthanide energy levels permitted by the non-zero orbital angular momentum in these ions, and the reduced symmetry of the electron distribution that results. We found this depopulation to be most pronounced for Co_2Ho. For the Er^{III} sample, the shape of $\chi_{mol}T$ is similar to that published[5] for the isostructural Dy^{III} compound. This result arises from the fact that both materials are Kramers ions (with total-spin angular momentum $J = 15/2$), a property which necessitates a bistable ground-state in each Er^{III} and Dy^{III} ion, implying that at low temperatures the magnetic properties in both samples will tend towards the behaviour of a two-level system.

The non-Kramers members of the series, Tb^{III} ($J = 6$) and Ho^{III} ($J = 8$), do not necessarily exhibit a ground-state doublet. However, the shape of $\chi_{mol}T$ for Co_2Tb resembles that of the Kramers ion samples in the series, whereas the shape for Co_2Ho is distinct in that $\chi_{mol}T$ decreases rapidly for temperatures below about 25 K. This result suggests that the ligand environment the around the Tb^{III} promotes a degenerate ground-state and a hence the similar

temperature dependence of the magnetic moment compared to Dy^{III} and Er^{III}. The pronounced down-turn in $\chi_{mol}T$ below 25 K for the Ho^{III} sample could indicate the energy level distribution is different compared to Tb^{III}, allowing for the possibility of a singlet ground state in Ho^{III}. We test this description of the lowest lying energy levels with low temperature AC susceptibility measurements (see below).

The DC magnetization of the four samples at 2 K is displayed in Fig. 6b. By comparing the measured moment parallel to the field at $\mu_0 H = 7$ T (of these powdered samples), to the expected saturation moment (Table 3), we find significantly reduced moments per ion in the case of Er^{III}, Tb^{III} and Ho^{III}. This supports the presence of single-ion anisotropy on an energy scale much larger than the Zeeman energy from the applied field, in agreement with the $\chi_{mol}T$ data.

For Co_2Gd, the magnetization (M) has been fitted to a Brillouin function (see for instance ref. 15), and since the orbital angular momentum is expected to be zero, the g-factor was fixed to $g = 2$. The resultant value of the total angular momentum was found to be $J = 3.3$, which is close to the value of 7/2 expected for Gd^{III} assuming the orbital moment to be zero for this complex. This result reinforces the conclusion that the system is paramagnetic down to 2 K, whereas the low temperature magnetization of the remaining samples cannot be accurately represented with a paramagnetic model.

Table 3. The saturation moment, $g_J J$, expected for Gd^{III}, Tb^{III}, Er^{III} and Ho^{III} compared to the measured moment at 2 K and 7 T, M ($\mu_0 H = 7$ T). In the absence of interactions between the lanthanide ions, the observation that the moment at 7 T is significantly less than saturation for Co_2Tb, Co_2Ho and Co_2Er indicates the presence of large magnetic anisotropy in these samples compared to the energy scale of the applied field.

Sample	$g_J J$ (μ_B)	$M(\mu_0 H = 7\ T)$ (μ_B)
Co_2Gd	7	6.5
Co_2Tb	9	4.4
Co_2Ho	10	4.7
Co_2Er	9	4.4

AC Susceptibility

The zero field AC susceptibility for Co_2Gd is shown in Fig. 7a and 7b. The in-phase component of susceptibility (χ') remained paramagnetic in form for temperatures down to 2 K and ac-frequencies up to 1500 Hz, which is emphasised by the fact that the out-of-phase component (χ'') is zero under these conditions. This implies that there is no energy barrier for changing the direction of the Gd^{III} moments, which further supports the suggestion that this material lacks single-ion anisotropy. Applying a $\mu_0 H_{DC} = 0.1$ T field induced a non-zero χ'' as the temperature is lowered (Fig. 7c and 7d). This effect becomes more pronounced, and persists to higher temperatures, when the frequency of the oscillating field is increased.

The effect of the DC-field on the measured AC susceptibility can be explained within the paramagnetic model. For a paramagnetic spin system in thermal equilibrium, a DC-field introduces anisotropy to the Hamiltonian and lifts the degeneracy of the m_J states of a free ion to produce a series of Zeeman levels (see e.g. ref. 15) populated with a Boltzmann distribution across the sample (here m_J is the z-component of the total angular momentum where the z-direction is defined to be parallel to the field). When an AC-field is applied to the system, the total-field at each ion continuously changes. This perturbation induces a net portion of the moments to reorientate, so as to occupy different m_J-levels and return the system to equilibrium.[16] On a local level, such a process can occur via interactions of the Gd^{III} ions with phonons.[16] As the temperature is lowered, the reduced probability of phonon interactions increases the time taken for the system to reach a new equilibrium state as the field changes, leading to an out-of-phase susceptibility. The temperature at which this effect

becomes measurable is expected to be higher for a larger AC-frequency, since the short time-scale of the oscillating field requires a fast relaxation mechanism for the spins to remain in phase with the AC-field.

The AC susceptibility of Co_2Er, recorded in zero-applied DC-field, is shown in Fig. 8a and 8b. On cooling, the in-phase component continuously rises, and below 5 K the out-of-phase component shows the AC-response is frequency-dependent, such that χ'' tends to be enhanced with increasing AC-frequency. At 2 K, however, χ'' begins to decrease for $f \geq 8000$ Hz. Overall, the small out-of-phase component and rising in-phase component are indicative of a fast relaxation mechanism for the Er^{III} moments. In addition, this relaxation rate is field dependent since the application of a DC-magnetic field induces χ' to exhibit a maximum, which tends to move to lower temperatures as the frequency of the AC-frequency is reduced (Fig. 8c). Furthermore, χ'' is significantly increased from the corresponding zero-field value (Fig. 8d), and for frequencies $f \geq 3000$ Hz, a maximum in χ'' is observed.

Since Er^{III} is a Kramers ion, we compare the AC susceptibility to that of the isostructural Dy^{III} compound,[5] a known SIM for which a maxima in χ' are also observed as the sample is cooled. These maxima occur at a temperature for which χ'' is increasing, and the out-of-phase component only showed a maximum itself as the temperature was cooled further. The similarity of the AC susceptibility of Co_2Er that of Co_2Dy is good evidence for SIM behaviour in the new Er^{III} material.

For Er^{III} ions in zero-field, there are two main competing relaxation pathways for the magnetization: (i) the quantum tunnelling of magnetization (QTM) between the two degenerate ground-states;[17] and (ii) an Orbach process in which an Er^{III} ion in one of the ground-states absorbs a phonon to overcome a thermal barrier, then emits a second phonon to decay to the degenerate ground state on the other side of the barrier.[18] In zero field, QTM

often dominates the relaxation of moments,[17] and this acts to suppress the out-of-phase component in a measurement of the AC susceptibility. When a DC-field is applied, the degeneracy of the ground state doublet is lifted, reducing the relaxation rate due to QTM and consequently increasing the influence of the relaxation process mediated by phonons, giving rise to the slow relaxation of moments at low temperatures.

To determine the number of active relaxation pathways present over the temperature range measured for the data collected with $\mu_0 H_{DC} = 0.1$ T, a Cole-Cole plot of χ' vs. χ'' for Co$_2$Er is constructed (Fig. 9). This shows that isotherms in the χ'-χ'' plane appear as single arcs, which become larger as the sample is cooled. This shape is indicative of phonon-relaxation via one relaxation pathway (see for instance ref. 18), and is analogous to the Dy^{III} sample.[5]

The data at 2.0, 2.6 and 3.0 K have been collated from repeat experiments, combining measurements recorded at temperatures which vary by ±100 mK along each of the respective arcs. Grouping the data in this way allows each arc to be fitted to the modified Debye model,[20] for which

$$\chi''(\chi') = -\frac{\chi_T - \chi_S}{2\tan\left[\frac{\pi}{2}(1-\alpha)\right]} + \sqrt{(\chi'-\chi_S)(\chi_T-\chi') + \frac{(\chi_T - \chi_S)^2}{4\tan^2\left[\frac{\pi}{2}(1-\alpha)\right]}} \qquad (1)$$

where χ_T is the isothermal susceptibility (measured in the DC-limit), χ_S is the adiabatic susceptibility (measured at high frequencies) and alpha measures the distribution of the relaxation time.[21] This form is expected to be obeyed for SIMs with a single relaxation pathway. The fits (solid lines in Fig. 9) are a good representation of the data and further supports the suggestion of SIM behaviour at low temperatures.

Having established a single phonon-assisted relaxation pathway, Arrhenius analysis can be used to estimate the size of the barrier to relaxation, U_{eff}. To do so, the temperature dependence of the relaxation time τ can be extracted from the data by applying the modified Debye model. Within this model, the maximum in χ'' vs. T (at constant f) occurs once the relaxation time satisfies the condition $\tau = 1/(2\pi f)$.[16] Strictly, this is true within Debye model if χ_T is assumed to be temperature independent,[16] which is a reasonable first approximation given that the peaks are observed over a narrow temperature window.

The maxima in χ'' vs. T from Fig. 8d are defined to be the temperature at which $d\chi''/dT = 0$, whilst the main source of error arises from the discreteness of the data. This error is estimated as half the interval between the two measured data points which fall either side of the maximum as defined above.

A plot of the logarithm of the relaxation time vs. inverse temperature of the peak in χ'' is shown in Fig. 10. The data can be modelled with the Arrhenius law, given by[18]

$$\ln \tau = \ln \tau_0 + \frac{U_{eff}}{k_B T} \qquad (2)$$

where τ_0 is the relaxation time measured in the high temperature limit. This law will be obeyed at high temperatures, where the high probability of phonon interactions ensures the Orbach relaxation mechanism dominates the sample's response to an ac-field. We expect that as the temperature is lowered, the relaxation rate will tend towards a temperature independent value as QTM becomes the prominent mechanism.

The measured relaxation time tends to increase on cooling, ruling out the scenario where QTM dominates the relaxation process. However, since the peaks in χ'' are only measured over narrow temperature range, this allows the data to be in two regimes: (i) a temperature window in which the Orbach process alone dominates, or (ii) an intermediate region between the two extremes where either phonon relaxation or QTM processes dominates.

This situation limits the quantitative conclusions that can be made. To emphasises this, we present two linear fits to the data, and the results are presented in Table 4. In linear fit 1, the high temperature portion of the data is fitted. On including the low temperature peaks in linear fit 2, the fitted value of the energy barrier is reduced, whilst the relaxation time increases. Higher AC-frequencies would be needed to differentiate between cases (i) and (ii) outlined above. This would push the peaks in χ'' to higher temperatures, and help determine whether the gradient of $\ln\tau$ vs. $1/T$ would become steeper, with a smaller τ-axis intercept, if the Arrhenius plot was extended to lower $1/T$. Given the experimentally available temperatures and frequencies, we therefore conclude that Co_2Er has $\tau_0 \leq 8 \times 10^{-7}$ s, and $U_{eff} \geq$ 9.9(8) K.

Table 4. Results of fitting the data in Fig. 10 to Eq. 2 over two temperature ranges.

Fit	$\ln \tau_0$	τ_0	U_{eff}/k_B (K)
Linear Fit 1	-14.1(3)	$\approx 8 \times 10^{-7}$	9.9(8)
Linear Fit 2	-13.4(2)	$\approx 2 \times 10^{-6}$	8.0(5)

The AC Susceptibility components of Co_2Tb, χ' and χ'', were investigated as a function of applied field at 2 K [Fig. 11a and 11b]. In contrast to Co_2Er, the data shows that the out-of-phase susceptibility of the Tb^{III} sample does not show a strong maximum as a function of frequency up to 10 kHz in a fixed applied DC-field of $\mu_0H_{DC} = 0.1$ T (dotted line 1). On increasing the DC-field beyond this point, the measurement of χ'' at 10 kHz reduces most

rapidly such that χ'' exhibits a maximum as a function of frequency in constant field. For $\mu_0 H_{DC} = 0.15$ T (dotted line 2), a strong signal can be measured, which shows a maximum in χ'' vs. f at the lowest temperatures accessible. As a result, this field is used to investigate the temperature dependence of the sample.

In zero applied DC-field, the in-phase susceptibility rises continuously on cooling [Fig. 12a]. This measurement is frequency independent, evident from a negligible out-of-phase component across the temperature range investigated and highlights that the system exhibits a fast relaxation of the Tb[III] moments [Fig. 12b]. In an applied-field of $\mu_0 H_{DC} = 0.15$ T [Fig. 12c and 12d] a large out-of-phase component is induced. This is consistent with a model in which the sample exhibits a doubly degenerate ground state, such that QTM dominates the relaxation process in zero-field. This fast relaxation is alleviated by the DC-field, allowing SIM behaviour to be observed. The applied field is large enough to induce peaks in χ'' at experimentally accessible temperatures and are observed below 3.5 K.

The maximain χ'' from these constant frequency measurements were extracted through differentiating the data (as described above) and an Arrhenius plot of the sample relaxation time is shown in Fig. 13. The data were fitted to the Eq. 2 over two separate temperature ranges, and the fitted parameters are displayed in Table 5. To aid in the interpretation of these results, a Cole-Cole plot is constructed [Fig. 11c] from constant temperature cuts to the AC susceptibility data in Fig. 12c and 12d.

Table 5. Results of fitting the data in Fig. 13 to Eq. 2 over two temperature ranges.

Fit	$\ln \tau_0$	τ_0	U_{eff}/k_B (K)
Linear Fit 1	-15.9(1)	$\approx 1 \times 10^{-7}$	15.6(4)
Linear Fit 2	-15.1(1)	$\approx 3 \times 10^{-7}$	13.3(3)

On cooling to 3 K, the arcs mapped out by isotherms in the χ'-χ'' plane become increasing large in a comparable manner to Co_2Er and Co_2Dy,[5] whilst below 2.5 K they begin to contract. To investigate this behaviour, the data below 3.5 K were fitted to Eq. 1 and the resultant fitted parameters given in Table 6.

The four isotherms in the range 2 to 3.5 K are well represented with the modified Debye model, indicating the sample behaves as a SIM with a unique thermally activated relaxation pathway. The value of α, which models the distribution of the relaxation time, increases on cooling. Given this, and combining it with the observation that the out-of-phase component is reduced at low temperatures, indicates that the sample behaviour below 2.5 K is increasingly influenced by an additional non-thermally activated relaxation mechanism, such as QTM. This is known to be present in the sample following the discussion of Fig. 12.

The Arrhenius plot, however, was relatively insensitive to a change in sample behaviour at 2.5 K. Nevertheless, the parameters extracted from the high-temperature portion of the data (Linear Fit 1 in Fig. 13) are less influenced by the possible onset of the additional relaxation mechanisms that emerge at low temperatures, therefore we estimate $\tau \leq 1 \times 10^{-7}$ s and $U_{eff} \geq$ 15.6(4) K for Co_2Tb.

Our conclusion that the non-Kramers ion Tb^{III} exhibits a ground state doublet can be discussed in terms of the ligand environment developed for the compounds in this study. Generally, a doublet ground state is permitted providing the ligand field around the Tb^{III} ion is strictly axial.[14,22] In the case of Co_2Tb, the Tb^{III} ions occupy specific positions in the monoclinic ($C2/c$) unit-cell where the point group is determined to be 2. This 2-fold rotational, or axial, symmetry of the ligand-field permits a doubly degenerate ground-state for the Tb^{III} ions.

Table 6. Results of fitting the isotherms for $2 \leq T \leq 3.5$ K in Fig. 11c to Eq 1.

Temperature (K)	$10^6 \chi_S$ (m^3 mol^{-1})	$10^5 \chi_T$ (m^3 mol^{-1})	α
3.5	3.0 ± 0.4	3.183 ± 0.008	0.226 ± 0.006
3.0	2.3 ± 1.0	3.514 ± 0.009	0.28 ± 0.02
2.5	2.9 ± 0.5	3.758 ± 0.006	0.323 ± 0.009
2.0	4.3 ± 0.4	3.644 ± 0.008	0.35 ± 0.01

The AC susceptibility of Co$_2$Ho, measured in zero DC-field, is shown in Fig. 14a and 14b. We find that χ' increases as the sample is cooled, and the measurement above 3 K is insensitive to the AC-frequencies ≤ 1000 Hz. Below 3 K, a weak frequency-dependence of the magnetic properties is evident in χ'', which tends to increases with ac-frequency. We note the out-of-phase response is two orders of magnitude weaker than that of Co$_2$Er, which we attribute to the relaxation rate in Co$_2$Ho being comparatively fast in the measured temperature range. Furthermore, under the application of a small DC-field [Fig. 14c and 14d] the data strongly resemble the corresponding measurements in zero-field, showing that the relaxation rate is field independent. This absence of measurable field-induced behaviour is likely to result from the energy-level structure in the non-Kramers Ho[III] ion and is a direct contrast to the Tb[III] sample.

The conclusions from DC susceptibility and magnetization measurements [Fig 6(a) and 6(b)] point to the presence of single-ion anisotropy in Co$_2$Ho which is of a comparable energy scale that seen in the Tb[III] and Er[III] complexes. To reconcile this with the field-independent relaxation rate in this sample, the implication is that QTM is not the dominant relaxation mechanism in zero-field. This can occur for the non-Kramers Ho[III] ions, if each ion exhibits a singlet ground-state. Such a state would necessarily have a $m_J = 0$ quantum number, which has easy-plane anisotropy and (in the classical picture) results in no energy barrier to

reorientate the moment within this plane (here m_J is the z-component of the total angular momentum, where the z-axis is defined by the local ligand field). This leads to a small out-of-phase component of the susceptibility that would be unaffected by an applied field,[23] providing the energy scale of the CEF producing the singlet ground state is much larger than the applied field, a condition which the DC magnetometry indicates is satisfied. Furthermore, the absence of field induced SIM behaviour has been an indicator of a singlet ground-state for non-Kramers ions in similar systems.[23,24]

Magnetostructural Properies

The shared structural form of the distorted monocapped square-antiprism $Ln^{III}O_9$ coordination sphere for each compound is shown in Fig. 15. The Ln^{III} ion occupies a site with point group 2, where the rotation axis is aligned along [010] such that there are five unique Ln^{III}-O distances within the coordination sphere. These distances are labelled (a)-(e) in the figure and are given for compounds **1-4** in Table 7. For comparison, the values for the published[5] isostructual single-ion magnet, $Co^{III}{}_2Dy^{III}$ [$U_{eff} = 88(8)$ K], are also given.

Table 7. Ln^{III}-O distances for compounds **1-4** using the labelling scheme given in Fig. 15. The results are compared to the published[5] material $Co^{III}{}_2Dy^{III}$ in the last column. The last row gives the average (standard deviation) of the nine Ln^{III}-O distances as measure of the size of the coordination sphere.

O label	(1) Gd^{III}	(2) Tb^{III}	(3) Ho^{III}	(4) Er^{III}	Dy^{III}
			Ln^{III}-O Distance (Å)		
(a)	2.398(5)	2.383(9)	2.388(6)	2.361(6)	2.383(9)
(b)	2.360(3)	2.334(6)	2.316(3)	2.312(3)	2.334(6)
(c)	2.687(3)	2.699(6)	2.700(3)	2.706(3)	2.699(6)

(d)	2.389(3)	2.370(6)	2.353(3)	2.338(3)	2.370(6)
(e)	2.385(2)	2.374(6)	2.352(2)	2.347(3)	2.374(6)
Average	2.444(1)	2.432 (0)	2.422(1)	2.410(1)	2.432 (0)

The Ln^{III}-O distances are similar in magnitude across each row of Table 7 implying there are only weak distortions of the geometry of the coordination sphere across this series of compounds. Moreover, the size of the coordination sphere parameterised by the average Ln^{III}-O distance is comparable for all five compounds. We therefore conclude that the magnitude of the axial CEF at the Ln^{III} sites is likely to be similar in each case such that the principal factor that determines the magnetic properties of the samples will be how this CEF field interacts with the with the unique 4f electron cloud distribution of each lanthanide ion.[14]

It has been reported that uniaxial single-ion properties for lanthanide ions with oblate free electron distributions can be encouraged for sandwich-like geometries of the surrounding ligands.[14] The square-antiprism arrangement of ligands in the compounds here provides such an environment, as is advocated by the Kramers system $Co^{III}_2Dy^{III}$ in which this coordination geometry led to uniaxial SIM behaviour with $U_{eff} = 88(8)$ K.[5] The Tb^{III} ion also has an oblate electron cloud, so given that uniaxial anisotropy was promoted for Dy^{III} in a similar coordination sphere, it follows that the CEF interaction in the Tb^{III} sample will result in a similar nature of the anisotropy of the sample. This is consistent with the suggestion for uniaxial behaviour of this new system in the section above.

Despite this, the thermal energy barrier in $Co_2^{III}Tb^{III}$ is smaller than in the Dy^{III} material, with a lower bound estimated to be 15.6(4) K. This result may be associated with the symmetry of

the CEF at the Ln^{III} sites. Whilst the 2-fold rotation symmetry of the coordination sphere was sufficient to promote a relatively large thermal barrier within the Kramers ion Dy^{III}, for which a degenerate ground-state is guaranteed, the non-Kramers Tb^{III} ions additionally require a strictly axial crystal-field in order to obtain a bistable ground state.[14] The point group at the Tb^{III} lattice sites of 2 is a low-symmetry environment, and this weakly axial lattice site is likely to lead to the smaller barrier for the Tb^{III} congener.

As discussed in the previous section, the spherical 4f electron cloud for Gd^{III} resulted in no measureable single-ion anisotropy for $T > 2$ K in this material. By comparison to Tb^{III} and Dy^{III}, both Er^{III} and Ho^{III} have only weakly prolate and oblate distortions of the 4f electron clouds repectively.[14] By analogy with the results of the Gd^{III} sample, we therefore expect weaker single-ion properties for these two materials given the similarity of the local lanthanide ion environments in each compound. In the case of Er^{III}, this argument is consistent with the energy barrier being the smallest of the uniaxial SIMs in this series. Furthermore, the weak SIM behaviour is in keeping with the result that the coordination geometry of the Ln^{III}-O_9 environments promotes strong single-ion behaviour in oblate ions, such that the prolate distortion within the Er^{III} 4f electron distribution is suboptimal for uniaxial behaviour. An equatorial ligand geometry[14] with a high degree of rotational symmetry is preferable to observe SIM behaviour for this ion. For Ho^{III}, the combination of the non-Kramers ion in the weakly axial ligand environment coupled with the more isotropic electron distribution relative to Tb^{III} may result in the lack of uniaxial behaviour being detected for this ion in this particular ligand environment.

Conclusion

In summary, we have utilized a compartmental ligand, 2-methoxy-6-[{2-(2-hydroxyethylamino)ethylimino}methyl] phenol (LH_3), to synthesize the heterometallic SIM containing a Co^{III} diamagnetic metal ion. We have measured the DC and AC susceptibility of four lanthanide containing complexes Co_2Ln^{III} (Ln = Gd^{III}, Tb^{III}, Ho^{III} and Er^{III}). Co_2Gd is well represented by a paramagnet model in the temperature range $2 \leq T \leq 300$ K, which we attribute to the spherical symmetry of the spin-only $^8S_{7/2}$ ground-state. This in turn leads to no single-ion anisotropy in this sample. The DC magnetic properties of this material therefore allow us to conclude that there are only weak interactions between lanthanide centres in these complexes such that the magnetic properties are determined by the single-ion behaviour of the lanthanide ions alone. The DC magnetic properties of Co_2Tb, Co_2Ho and Co_2Er all suggest the presence of crystalline-electric field splitting of the energy levels which is ≈ 100 K.

The non-Kramers ion Co_2Tb shows evidence for field induced SIM properties emerging at low temperatures, which results from the axial ligand field at the Tb^{III} sites permitting a bistable ground state necessary for SIM behaviour. We estimate an energy barrier of $U_{eff} \geq$ 15.6(4) K for this sample. The similarity of the zero-field and in-field AC susceptibility of Co_2Ho suggests lowest lying energy level is the $m_J = 0$ state, such that quantum tunnelling of magnetization is not present as a relaxation mechanism in this compound. Co_2Er shows strong evidence for field induced SIM behaviour and we suggest the energy barrier is $U_{eff} \geq$ 9.9(8) K.

Acknowledgements

Electronic supplementary information (ESI) available: Cif files for **1-4** (CCDC no. 1429323-1429326), additional figures, BVS calculation table bond length and bond angles tables.

References

1. (a) J. W. Sharples and D. Collison, *Coord. Chem. Rev*., 2014, **260**, 1-20; (b) J. Goura, R. Guillaume, E. Rivière and V. Chandrasekhar, *Inorg. Chem*., 2014, **53**, 7815-7823; (c) P. Bag, J. Goura, V. Mereacre, G. Novitchi, A. K. Powell and V. Chandrasekhar, *Dalton Trans*., 2014, **43**, 16366-16376; (d) C. Meseguer, S. Titos-Padilla, M. M. Hänninen, R. Navarrete, A. J. Mota, M. Evangelisti, J. Ruiz and E. Colacio, *Inorg. Chem*., 2014, **53**, 12092-12099; (e) E. Colacio, J. Ruiz-Sanchez, F. J. White and E. K. Brechin, *Inorg. Chem*., 2011, **50**, 7268-7273; (f) M. Hołyńska, D. Premužić, I. R. Jeon, W. Wernsdorfer, R. Clérac and S. Dehnen, *Chem. Eur. J.*, 2011, **17**, 9605-9610; (g) V. Mereacre, D. Prodius, Y. Lan, C. Turta, C. E. Anson and A. K. Powell, *Chem. Eur. J*., 2011, **17**, 123-128; (h) K. C. Mondal, A. Sundt, Y. Lan, G. E. Kostakis, O. Waldmann, L. Ungur, L. F. Chibotaru, C. E. Anson and A. K. Powell, *Angew. Chem. Int. Ed*., 2012, **51**, 7550-7554; (i) S. K. Langley, D. P. Wielechowski, V. Vieru, N. F. Chilton, B. Moubaraki, L. F. Chibotaru and K. S. Murray, *Chem. Sci.*, 2014, **5**, 3246-3256.

2. (a) I. Oyarzabal, J. Ruiz, J. M. Seco, M. Evangelisti, A. Camón. E. Ruiz, D. Aravena and E. Colacio, *Chem. Eur. J.*, 2014, **20**, 1; (b) S. Titos-Padilla, J. Ruiz, J. M. Herrera, E. K. Brechin, W. Wersndorfer, F. Lloret and E. Colacio, *Inorg. Chem.*, 2013, **52**, 9620; (c) M. A. Palacios, S. Titos-Padilla, J. Ruiz, J. M. Herrera, S. J. A. Pope, E. K. Brechin and E. Colacio, *Inorg. Chem.*, 2014, **53**, 1465; (d) S. M. T. Abtab, M. C. Majee, M. Maity, J. Titiš, R. Boča and M. Chaudhury, *Inorg. Chem.*, 2014, **53**, 1295; (e) A. Yamashita, A. Watanabe, S. Akine, T. Nabeshima, M. Nakano, T. Yamamura and T. Kajiwara, *Angew. Chem., Int. Ed.*, 2011, **50**, 4016; (f) J. Ruiz, G. Lorusso, M. Evangelisti, E. K. Brechin, S. J. A. Pope and E. Colacio, *Inorg. Chem.*, 2014, **53**, 3586; (g) C.-M. Liu, D. -Q. Zhang, X. Hao and D. -B. Zhu, *Chem. Asian J.*, 2014, **9**, 1847; (h) S. K. Langley, N. F. Chilton, B. Moubaraki and K. S. Murray, *Inorg. Chem*., 2013, **52**, 7183.

3. A. Upadhyay, S. K. Singh, C. Das, R. Mondol, S. K. Langley, K. S. Murray, G. Rajaraman and M. Shanmugam, *Chem. Commun.*, 2014, **50**, 8838.

4. (a) V. Chandrasekhar, B. M. Pandian, R. Azhakar, J. J. Vittal and R. Clérac, *Inorg. Chem*., 2007, **46**, 5140-5142; (b) V. Chandrasekhar, B. M. Pandian, J. J. Vittal and R. Clérac, *Inorg. Chem.*, 2009, **48**, 1148-1157.

5. J. Goura, J. Brambleby, P. Goddard and V. Chandrasekhar, *Chem. Eur. J*., 2015, **21**, 4926-4930.

6. A. J. Brown, D. Pinkowicz, M. R. Saber and K. R. Dunbar, *Angew. Chem. Int. Ed.*, 2015, **54**, 5864-5868.

7. A. R. Tatchell, B. S. Furnis, A. J. Hannaford and P. W. G. Smith, *Vogel's Textbook of Practical Organic Chemistry, 5th ed.*; Longman: London, 1989.

8. (a) F.-M. Wang, *ActaCryst.*, 2012, **E68**, m26; (b) Z.-L. You, D.-H. Shi, J.-C. Zhang, Y.-P. Ma, C. Wang and K. Li, *Inorg. Chim. Acta.*, 2012, **384**, 54.

9. (a) *SMART & SAINT Software Reference manuals*, Version 6.45; Bruker Analytical X-ray Systems, Inc.: Madison, WI, 2003. (b) Sheldrick, G. M. SADABS, a software for empirical absorption correction, Ver. 2.05; University of Göttingen, Göttingen, Germany, 2002. (c) G. M. Sheldrick, *Acta Crystallogr., Sect. A: Fundam. Crystallogr.,* 2008, **64**, 112; (d) G. M. Sheldrick, *SHELXTL Version* **2014/7.** http://shelx.uni-ac.gwdg.de/SHELX/index.php.; (e) C*rystal Structure Refinement: A Crystallographer's guide to SHELXL*, ed. P. Muller, International Union of Crystallography and Oxford University Press, 2006. (f) L. J. Farrugia, *J. Appl. Crystallogr.* **1999,** 32, 837; (g) L. J. Farrugia, *WinGX, version 1.65.04, Department of Chemistry, University of Glasgow, Glasgow, Scotland,* **2003***,* (h) L. J. Farrugia, *J. Appl. Crystallogr.* **2012,** 45, 849-854; (i) A. L. Spek, *Acta Crystallogr. C Struct. Chem.* **2015,** 71, 9-18; (j) Bradenburg, K. *Diamond*, *Ver. 3.2k*; Crystal Impact GbR: Bonn, Germany, **2015**.

10. (a) G. Wu, I. J. Hewitt, S. Mameri, Y. Lan, R. Clérac, C. E. Anson, S. Qiu and A. K. Powell, *Inorg. Chem.*, 2007, **46**, 7229; (b) P. Bhowmik, N. Aliaga-Alcalde, V. Gómez, M. Corbella and S. Chattopadhyay, *Polyhedron*, 2013, **49**, 269; (c) Y.-Z. Zheng, Y. Lan, C. E. Anson and A. K. Powell, *Inorg. Chem.*, 2008, **47**, 10813.

11. J. Goura, V. Mereacre, G. Novitchi, A. K. Powell and V. Chandrasekhar, *Eur. J. Inorg. Chem.*, 2015, 156-165.

12. (a) I. D. Brown and K. K. Wu, *ActaCrystallogr.*, 1976, **B32***,* 1957; (b) W. Liu and H. H. Thorp, *Inorg. Chem.*, 1993, **32**, 4102; (c) R. M. Wood and G. J. Palenik, *Inorg. Chem.*, 1998, **37***,* 4149; (d) I. D. Brown and D. Altermatt, *Acta Cryst.*, 1985, **B41**, 244.

13. G. A. Bain and J. F. Berry, *J. Chem. Edu.*, 2008, **85**, 532.

14. J. D. Rinehart and J. R. Long, *Chem. Sci.*, 2011, **2**, 2078.

15. S. J. Blundell, *Magnetism in Condensed Matter*, OUP: Oxford, 2011.

16. D. Gatteschi, R. Sessoli and J. Villain, *Molecular Nanomagnets,* Oxford University Press, 2006, 69-75.

17. D. Woodruff, R. Winpenny and R. Layfield *Chem. Rev.*, 2013, **113**, 5110.

18. A. Morrish, *The Physical Properties of Magnetism*, Wiley: New York, 1965, 90-101.

19. R. Blagg, L. Ungur, F. Tuna, J. Speak, P. Comar, D. Collison, W. Wernsdorfer, E. McInnes, L. Chibotaru and R. Winpenny, *Nature Chem.*, 2013, **5**, 673.

20. M. Hagiwara, *J. Magn. Magn. Mat.*, 1998, **117-181**, 81.

21. K. Cole and R. Cole, *J. Chem. Phys.*, 1941, **9**, 341.

22. N. Ishikawa, M. Sugita, T. Ishikawa, S. Koshihara and Y. Kaizu, *J. Am. Chem. Soc.*, 2003, **125**, 8694.

23. M. Sugita, N. Ishikawa, T. Ishikawa, S. Koshihara and Y. Kaizu, *Inorg. Chem.*, 2006, **45**, 1299.

24. S. Jiang, S. Liu, L. Zhou, B. Wang, Z. Wang and S. Gao, *Inorg. Chem.*, 2012, **51**, 3079.
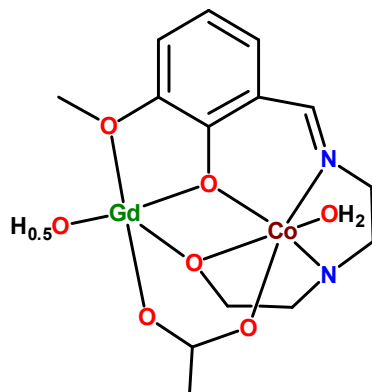
Chart 2. Asymmetric unit of complex **1**
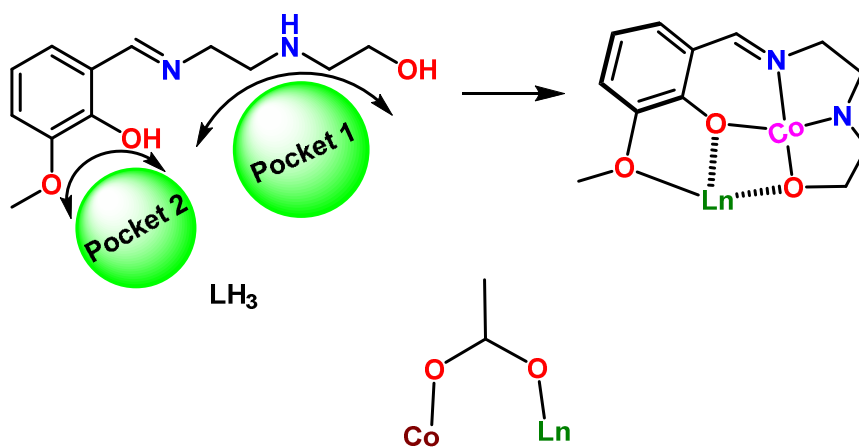
Chart 3. Coordination binding modes of L^{3-} and $MeCO_2^{-}$ ligands in the present study.
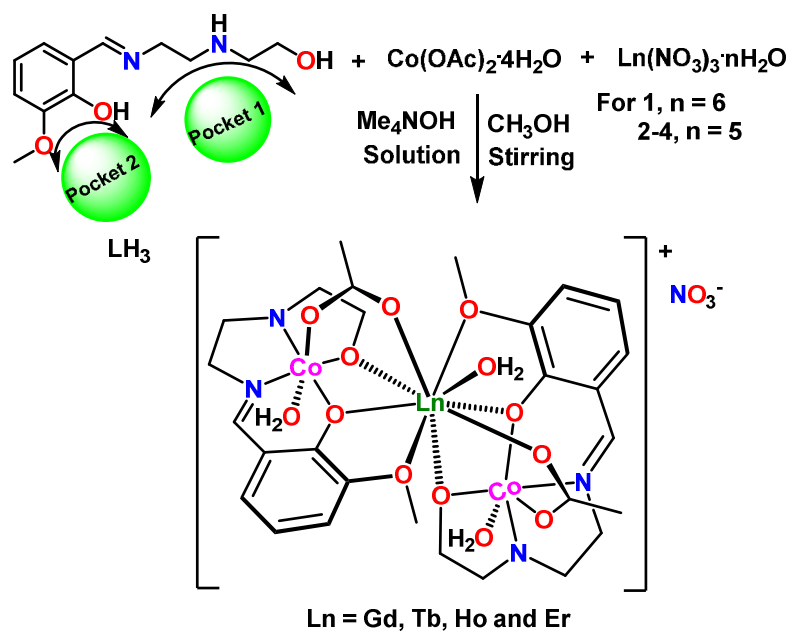
Scheme 1. Synthesis of the trinuclear heterometallic complexes **1-4**
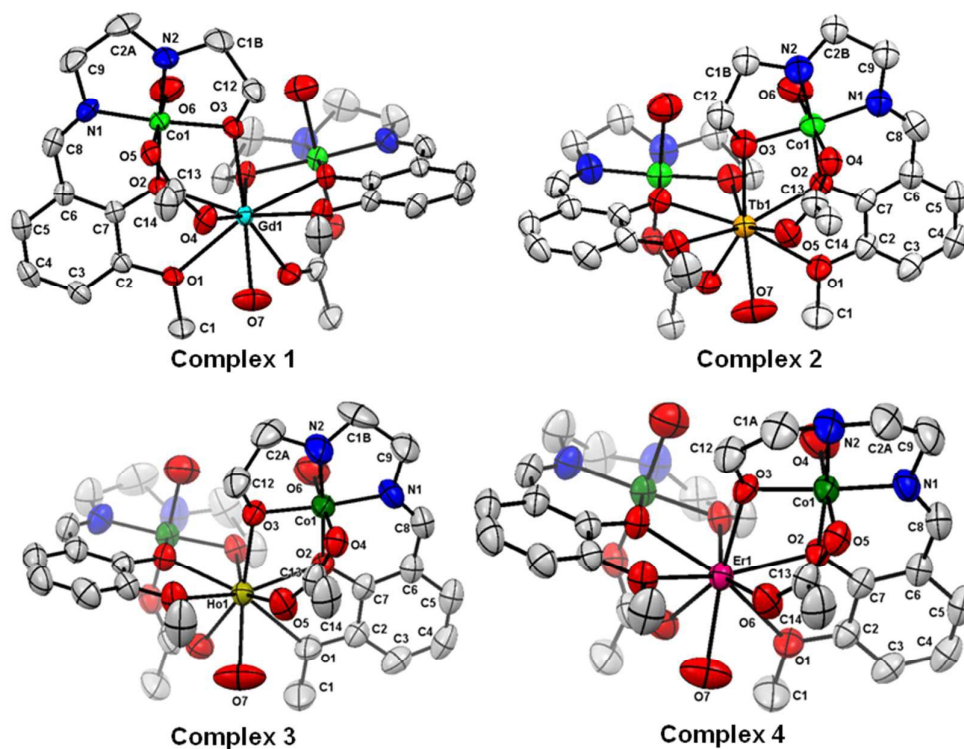
Fig. 1. ORTEP diagrams (with 50% ellipsoid probability) of **1−4**. The atoms of the asymmetric units are labelled. Disordered parts/ H atoms/ anion/ solvent molecules are omitted for clarity. Colour codes: Gd = cyan; Tb = orange; Ho = yellow; Er = pink, Co = green, O = red; N = blue and C = light-grey.
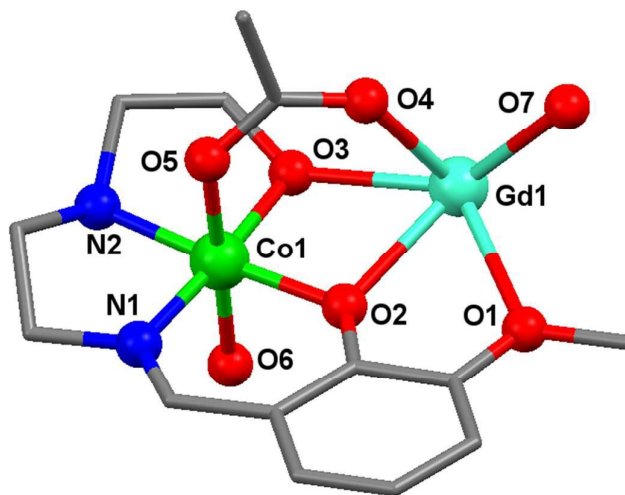
Fig. 2. Asymmetric unit of **1**. The coordinated atoms and the metal centres are highlighted with ball-and-stick model. Hydrogen atoms and other disordered part/ anion/ solvent molecules are omitted for clarity. Colour code: C = grey.

(a) (b)
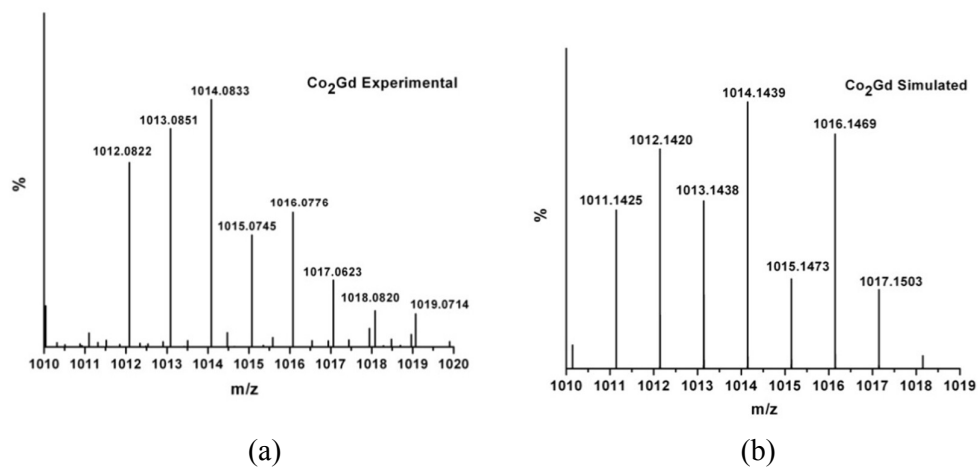
Fig. 3. (a) ESI-MS spectrum of complex **1** (Experimental) and (b) Simulated isotopic pattern

for the parent ion peak of **1**

(a) (b)
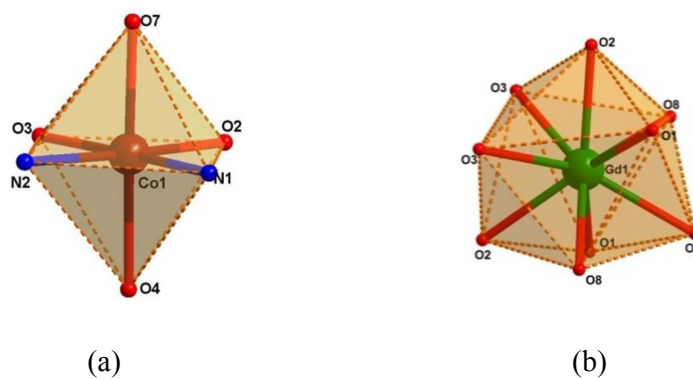
Fig. 4. Coordination geometry around the metal centers (a) Co^{III} center distorted octahedron
and (b) Gd^{III} center distorted monocapped square anti-prism geometry in **1**
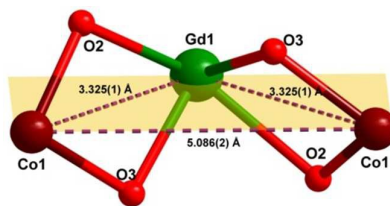
Fig. 5. Mean planes of **1**. Isosceles triangular arrangement of the metal ions
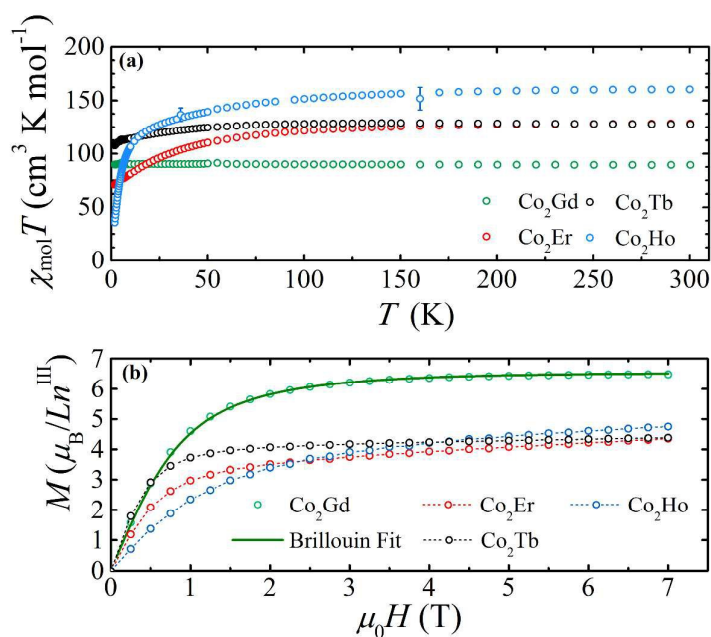
Fig. 6. (a) The product $\chi_{mol}T$ vs. temperature, T, for Co_2Gd, Co_2Tb, Co_2Er and Co_2Ho. The Gd^{III} sample remains paramagnetic down to 2 K, whilst for the remaining samples, $\chi_{mol}T$ is approximately constant at room temperature and begins to decrease below about 100 K, which we attribute to the thermal depopulation of crystalline electric field split levels in the lanthanide ions. A diamagnetic correction of -6.0×10^{-9} m^3 mol^{-1} for **1**, and -6.1×10^{-9} m^3 mol^{-1} for **2-4** was subtracted from the susceptibility data, estimated from Ref. 13. (b) Magnetization (in Bohr magnetons per lanthanide ion) vs. applied field for Co_2Gd, Co_2Tb, Co_2Ho and Co_2Er at 2 K. The solid line is a fit to a Brillouin function. The dotted lines are a guide to the eye.
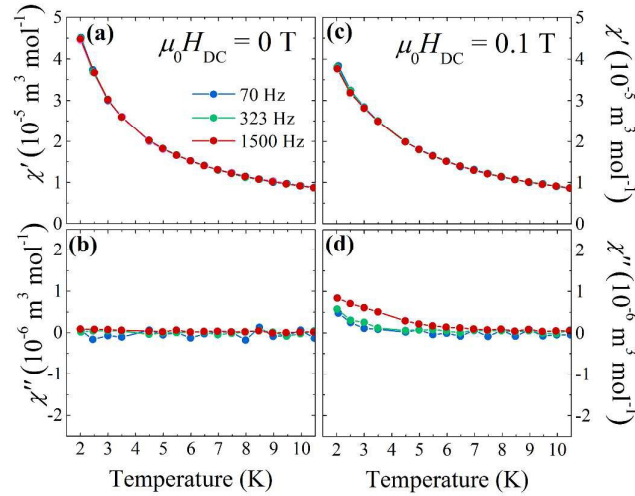
Fig. 7. AC susceptibility vs. temperature for Co$_2$Gd. In-phase (a) and out-of-phase (b) susceptibility vs. temperature with μ_0H_{DC} = 0 T and μ_0H_{AC} = 0.4 mT. (Note the change in scale). In-phase (c) and out-of-phase (d) components vs. temperature under the application of a DC-field μ_0H_{DC} = 0.1 T. The colours indicate data collected with different frequencies for the oscillating field.
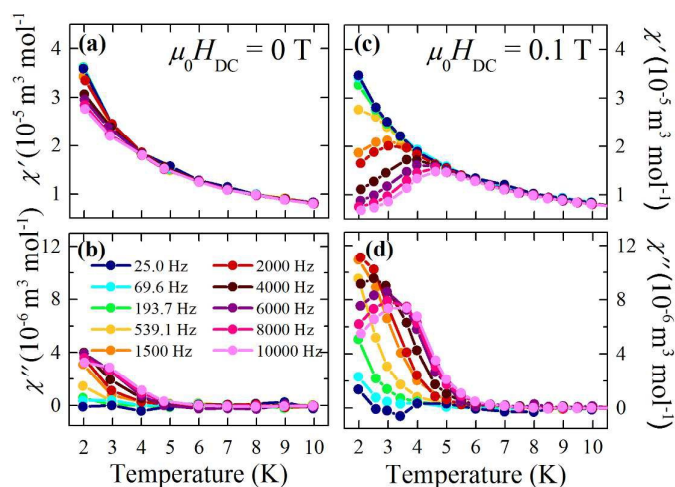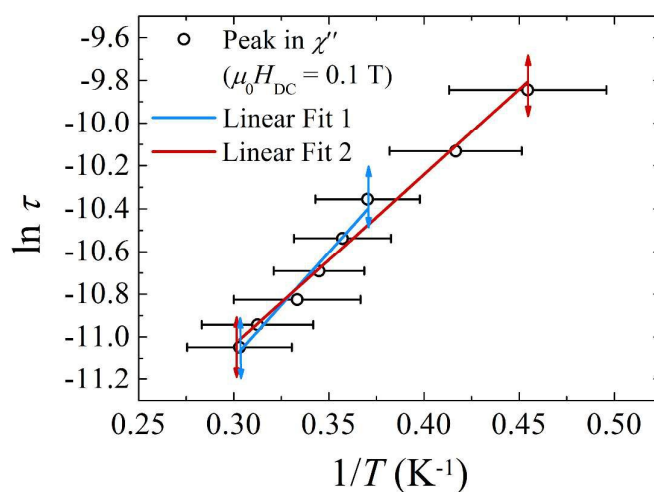
Fig. 8. (a) In-phase susceptibility vs. temperature for Co_2Er in zero DC field. (b) Corresponding out-of-phase susceptibility vs. temperature for Co_2Er. (c) In-phase susceptibility vs. temperature for Co_2Er in an applied DC field, $\mu_0H_{DC} = 0.1$ T. (d) Corresponding out-of-phase susceptibility vs. temperature for Co_2Er. The colours indicate data collected with different AC-frequencies.
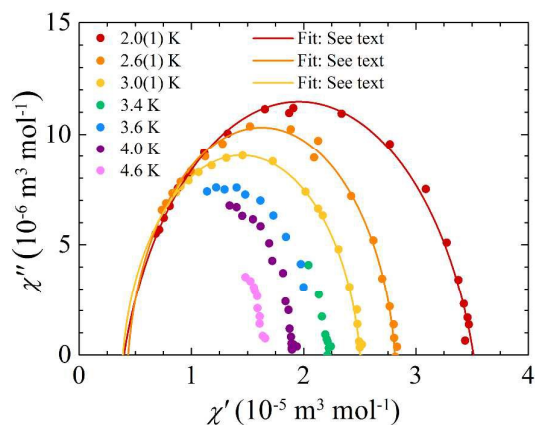
Fig. 9. Cole-Cole plot of the AC Susceptibility data for Co_2Er collected in $\mu_0H_{DC} = 0.1$ T. For each isotherm, frequency increases on moving from the isothermal limit, where χ' is greatest, towards the adiabatic limit as χ' decreases. The solid lines are free fits to Eq. 1. The fitted value of χ_S was found to be approximately temperature independent, with an average value of $\chi_S = 0.42(2) \times 10^{-5}$ m^3 mol^{-1}, whilst α varied from 0.2 to 0.1 for temperatures from 2.0 to 3.0 K.

Fig. 10. Logarithmic plot of the relaxation time τ versus inverse temperature for Co_2Er in a DC field of $\mu_0H_{DC} = 0.1$ T, as measured from the position of the peak in χ'' vs. T in Fig. 8d. The data were fitted to Eq. 2 over two temperature ranges and the results are given in Table 4.
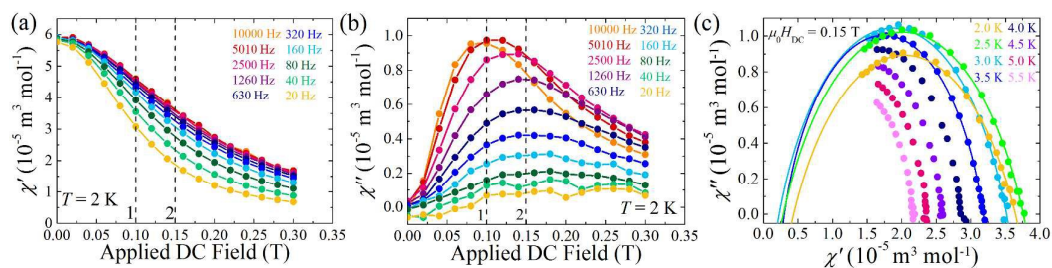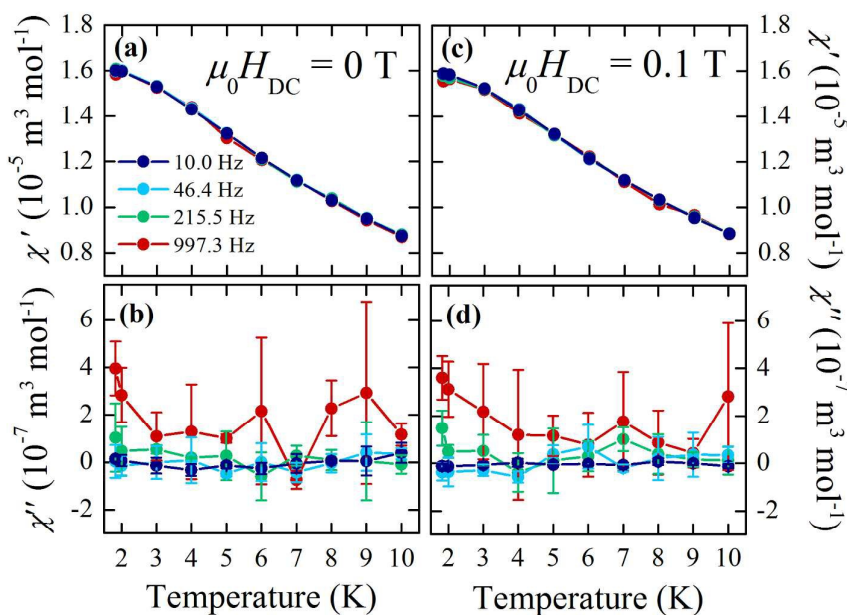
Fig. 11. (a) In-phase susceptibility vs. applied DC-field for Co_2Tb at 2 K for selected frequencies in the range $20 \leq f \leq 10000$ Hz. (b) Out-of-phase susceptibility vs. applied DC-field for Co_2Tb. χ'' exhibits a maximum as a function of frequency for fixed applied DC fields $\mu_0H_{DC} \geq 0.1$ T. **(c)** Cole-Cole plot of Co_2Tb collected in $\mu_0H_{DC} = 0.15$ T. Isotherms for $T \leq 3.5$ K have been fitted to Eq. 1, with the resultant parameters displayed in Table 6.
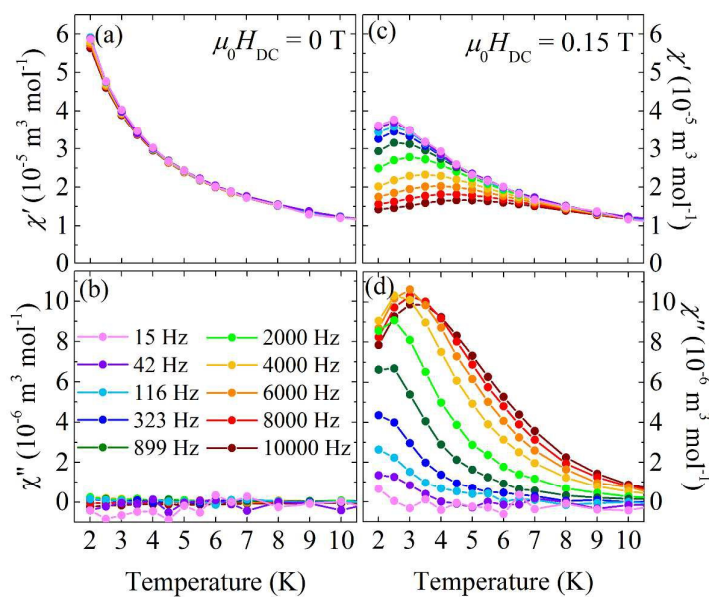

Fig. 12. AC susceptibility vs. temperature for Co_2Tb. (a) In-phase susceptibility vs. temperature for Co_2Tb in zero DC field. (b) Corresponding out-of-phase susceptibility vs. temperature for Co_2Tb. (c) In-phase susceptibility vs. temperature for Co_2Tb in an applied DC field, $\mu_0H_{DC} = 0.15$ T. (d) Out-of-phase susceptibility vs. temperature for Co_2Tb, with $\mu_0H_{DC} = 0.15$ T. The colours indicate data collected with different AC-frequencies.
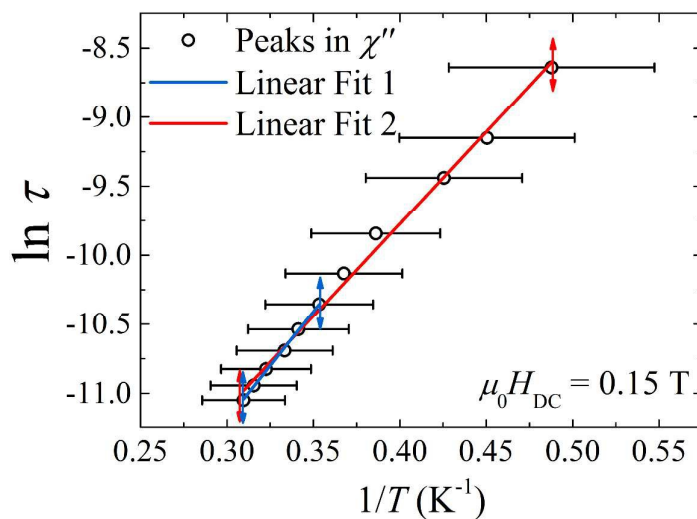
Fig. 13. Logarithm of the sample relaxation time vs. inverse temperature for Co_2Tb. The data have been fitted to Eq. 2 over two temperature regions and the resultant parameters extracted from the fits are given in Table 5.

Fig. 14. (a) In-phase susceptibility vs. temperature for Co_2Ho in zero DC field. We see a very weak frequency dependence of the in-phase component only below $T \lesssim 3$ K. (b) Out-of-phase susceptibility vs. temperature for Co_2Ho. Note the change in scale. In-phase (c) and out-of-phase (d) susceptibility vs. temperature for Co_2Ho in applied DC-field $\mu_0 H_{DC} = 0.1$ T. The colours indicate data collected with different AC-frequencies.
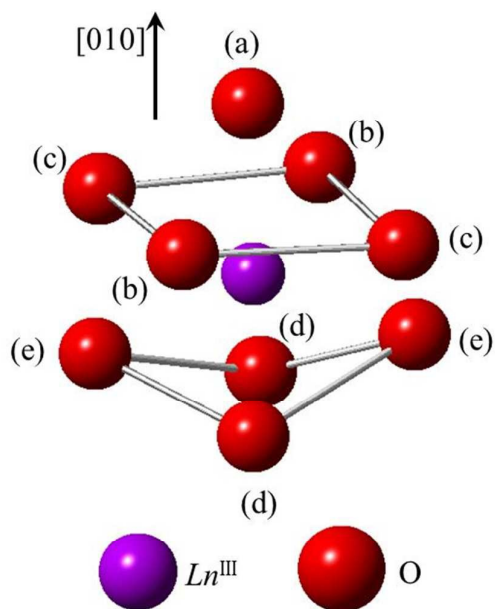
Fig. 15 The monocapped distorted square antiprism arrangement of the O_9 coordination sphere around each Ln^{III} ion. The Ln^{III} occupy sites with a point group of 2 where the rotation axis along [010] such that there are five unique Ln^{III}-O distances, labelled with (a)-(e).

Table of Contents

Heterometallic Trinuclear {Co$^{III}_2$Ln^{III}} (Ln = Gd, Tb Ho and Er) Complexes in a Bent Geometry. Field-induced Single-Ion Magnet Behavior of the Er^{III} and Tb^{III} Analogues

*Joydeb Goura,[a] Jamie Brambleby,[b] Craig V. Topping,[c] Paul A. Goddard,[*b] and Vadapalli Chandrasekhar*[*a,d]*
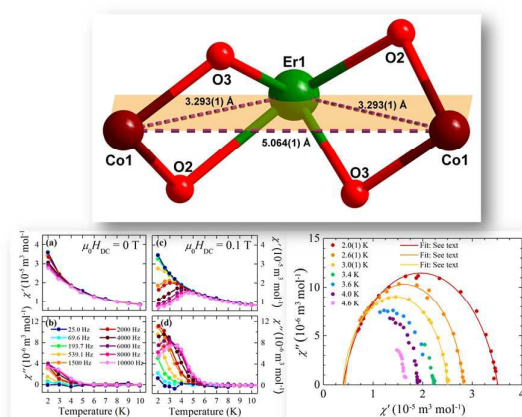
[a]Department of Chemistry, Indian Institute of Technology Kanpur, Kanpur-208016, India;

[b]Department of Physics, University of Warwick, Gibbet Hill Road, Coventry, CV4 7AL, United Kingdom;

[c]Department of Physics, Clarendon Laboratory, University of Oxford, Oxford, Parks Road, OX1 3PU, United Kingdom;

[d]National Institute of Science Education and Research, Institute of Physics Campus, Sachivalaya Marg, Sainik School, Bhubaneswar, Orissa - 751 005, India

E-mail: vc@iitk.ac.in; vc@niser.ac.in; p.goddard@warwick.ac.uk

In this paper we report the synthesis, structures and detailed magnetic properties of the heterometallic trinuclear Co^{III}Ln^{III} complexes. The metallic core of these complexes possesses a (Co^{III}-Ln^{III}-Co^{III}) motif which possesses a bent geometry. The magnetic properties of the complexes reveal that erbium and terbium analogues shows field-induced single-ion magnetic behaviour. The energy barrier for the reversal of the magnetization of Co$^{III}_2$Tb^{III} analogue is $U_{eff} \geq 15.6(4)$ K while the Co$^{III}_2$Er^{III} analogue $U_{eff} \geq 9.9(8)$ K.